A Mechanics-Based Model for a Tendon-Driven Active Needle Navigating inside a Multiple-Layer Tissue

Blayton Padasdao[1] and Bardia Konh[1]

***Abstract*— Percutaneous minimally invasive procedures such brachytherapy and biopsy require a flexible active needle for precise movement inside tissue and accurate placement at target positions. In previous work, we presented a tendon-driven active needle to navigate inside tissue. This work presents a new model to predict the deflection of the tendon-driven needle while steering in a multiple-layer soft tissue. A multi-layer phantom tissue with different localized stiffness was developed for needle insertion tests followed by indentation tests to identify its mechanical properties. Using a robot that inserts and actively bends the tendon-driven needle inside the soft tissue, various experiments were conducted for model validation. The proposed model was verified by comparing the simulation results to the empirical data. The results demonstrated the accuracy of the model in predicting the tendon-driven needle deflection in multiple-layer (different stiffness) soft tissue.**

***Index Terms*— Key words:** Active tendon-driven needle, mechanics-based model, real-time tracking, ultrasound tracking, robotic control

I. Introduction

Advanced robotic tools [1], [2] have been developed in recent decades to improve minimally invasive surgeries for diagnostic and therapeutic purposes. Endovascular and endoscopic procedures as well as needle-based procedures such as biopsy and brachytherapy have privileged from the improved dexterity and precise movement of the robotic instruments. The success of these procedures depends on (i) precise navigation of the tools around anatomical obstacles or sensitive organs, (ii) accurate targeting, and (iii) precise tracking of the tip and tracing the shape of the tools while navigating inside the patient. Common challenges in robotic manipulation and control include poor visualization, limited imaging possibilities, and lack of proper feedback (shape or force sensing) during the interventions [3], [4]. Recognizing the importance of precision tracking and placement, several efforts have been made in recent years to improve medical imaging and interventional instruments.

Prostate cancer is the most common cancer in American men. The American Cancer Society's estimates about 288,300 new cases of prostate cancer and 34,700 deaths from prostate cancer in the US alone in 2023. Early diagnosis of cancer followed by effective treatment plans are among factors that could improve cancer survival rates. Minimally invasive needle-based procedures are commonly used in prostate cancer biopsy and brachytherapy for diagnosis and treatment, respectively. Accurate cancer diagnosis relies on clinically significant biopsy samples extracted from the suspicious tissue that is marked by a radiologist. Precise sampling demands for accurate needle placements. Brachytherapy involves the use of needles to introduce radiation dose to the cancerous cells. This exudes a localized amount of radiation dose sufficient to destroy cancerous tissue. The procedure's outcome relies on precise needle placement close to the target cancerous tissue. However, manual needle placement inside tissue has been a challenging task, and therefore research efforts have been focused to develop robotic instruments to assist in needle placement. Robotic needle manipulation requires deep understanding of needle-tissue interactions. Viscoelastic and non-homogeneous tissue properties as well as dynamic interactive forces applied to the needle are among the factors to be considered in robotic needle insertion control. There have been several attempts to develop passive and active steering needles (some with self-sensing capabilities [5], [6]) to improve targeting accuracy. In a previous work, we presented an active steerable needle for prostate brachytherapy [7], as well as an active steerable core biopsy needle for prostate biopsy [8], [9].

On the other hand, medical imaging plays an important role in position tracking of medical devices while operating inside the patient's body. Surgeons rely on position tracking to accurately guide the needles in a desired trajectory towards the target location(s). Medical imaging provides online (intraoperative) trajectory tracking of the tip of the needle that can be used to estimate the deviation from the desired trajectory. Our group has presented a method to estimate the 3D shape of a steerable needle inside tissue using 2D ultrasound (US) images [10], and introduced a robot-assisted US tracking system along with 3D needle shape prediction to obtain the 3D position of the tip inside tissue [11].

Additionally, movement of the target and the tissue [12], viscoelastic properties of the tissue, and complex needle-tissue interactions are among the challenges in model-based feedback control of the robotic tools steering inside tissue. Mechanics-based models [13] have been developed in the past to predict the deflection of flexible passive needles [14] inside the tissue considering the tissue interaction forces at the tip and external lateral forces [15].

In this work, we present a new mechanics-based model to predict the bending of an active tendon-driven needle inside the tissue. The model is validated using insertion and manipulation experiments in multiple-later soft tissue. This work builds on our previous efforts involving manipulation and tracking of the active needle and introduces a new mechanics-based model to predict needle deflection based on needle-tissue interaction. The model is intended to be used in model-based control of the active needle inside tissue for minimally invasive procedures in future works.

II. Materials and Methods

A. Steerable Continuum Tendon-Driven Active Needle

Figure 1 shows the active needle, fabricated on a superelastic nitinol tube (1.80 and 1.50mm, outer and inner diameters, respectively), for model validation experiments. Figure 1a shows the needle's flexible section with a series of

[1] Department of Mechanical Engineering, University of Hawaii at Manoa, Honolulu, HI 96822, USA (emails: {blaytonp, konh}@hawaii.edu)

six notches with dimensions of 1.40mm deep and 0.30mm wide for improved flexibility. The flexure section was insulated using ultrathin heat shrink plastic to prevent tissue from penetrating inside the needle tube. Figure 1b shows the design parameters of each notch carved on the needle tube. Table 1 lists the design parameters, where r_o and r_i are the outer and inner radius of the needle, respectively, t and d are the width and depth of the cutouts, respectively, d_n is the distance between the two consequent cutouts, and $\bar{y}$ is the position of the neutral axis.

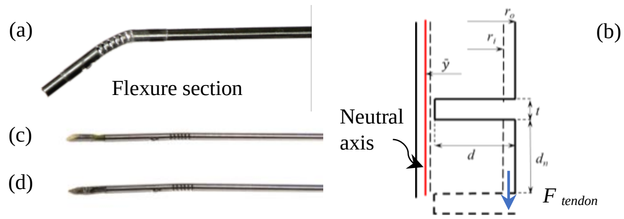

Figure 1. Tendon-driven active needle: (a) flexure section with insulating cover, (b) design parameters, (c) and (d) bevel-, and conical-tip, respectively.

The notches were made in the lab using typical machining tools such as a Dremel, and ultra-thin cut- off discs with a thickness of 0.30mm and 0.127mm (Gesswein & Co., Inc., Bridgeport, Connecticut). Based on our calculations (details are outlined in our previous work [34]), the estimated maximum bending angle of this needle is 60°. A 30° bevel-tip and a conical-tip stylets were made, as shown in Figures 1c and 1d, respectively, to facilitate initial puncture of the needle into the tissue.

Table 1. Design parameters of the active tendon-driven notched needle, shown in Figure 1. Dimensions are in mm.

r_o	r_i	t	d	d_n	$\bar{y}$
0.90	0.75	0.30	1.40	0.64	0.71

B. *Deflection Model of the Steerable Tendon-Driven Active Needle inside Soft Tissue*

This section discusses the tool-tissue interaction model based on Euler-Bernoulli beam theory [17] that predicts the tool's deflection inside a soft tissue. The input parameters to the model (see Figure 2) are the tip force F_t, and the tendon-pulling force F_p. The theory is valid for deflections that are smaller than 10% of the total length of the beam, which is the case for most of the minimally invasive interventions such as biopsy, brachytherapy, endovascular and endoscopic tools. The equations consider the energy stored in the bent tool, while steering inside the tissue, as well as the external work applied to the tool to form a potential function. The equations are then transformed into a linear system of equations using the Rayleigh-Ritz method [18].

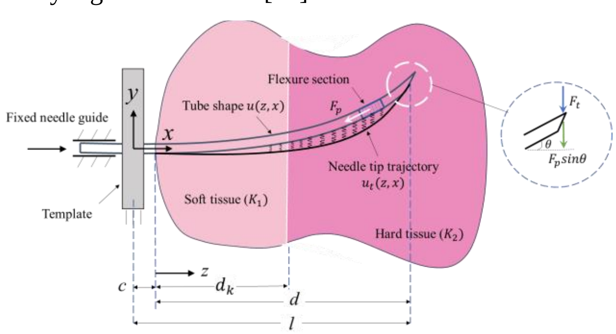

Figure 2. Mechanics of tendon-driven active needle inside soft tissue.

The equation below shows the overall potential energy of the system, which is a combination of the *energy stored in the bent robotic tool and tissue* as well as the *external work* applied to the robotic tool during an insertion task:

$$\Pi(u) = U(u) + V = U_s(u) + U_d(U) + V_t + V_p \quad (1)$$

in which $\Pi(u)$ is the total stored energy in the system, $U(u)$ is the energy stored in the system due to the tool displacement, V is the work applied to the system, U_s is the strain energy due to the bending of the robotic tool, U_d is the energy stored in the system due to displaced tissue, V_t is the work applied at the tip due to the tool-tissue interactions, and V_p is the work applied by the internal tendons of the robotic tool.

The strain energy stored in the system due to the bending of the robotic tool, U_s, can be obtained as follows:

$$U_s(u) = \int_0^l \frac{EI}{2}\left(\frac{\partial^2 u(d,z)}{\partial z^2}\right)^2 dz \quad (2)$$

where z is the horizontal coordinate, E is the Young's modulus, I is the tool's second moment of inertia, l is the tool length, d is the insertion depth, and $u(d,l)$ is the tool deflected shape at the end of the insertion.

$U_d(u)$ is the energy stored in the system due to the tissue displacement.

$$U_d(u) = \frac{K}{2}\int_0^l (u(d,z) - u_t(d,z))^2\, dz \quad (3)$$

where $u_t(d,l)$ is the measured path at the tip given by the medical imaging modality (e.g., ultrasound, CT, MRI) during the insertion task, and K is the tissue stiffness.

The work applied at the tip due to the tool-tissue interactions is:

$$V_t = F_t\, u(d,l) \quad (4)$$

where F_t is the tool tip force.

The work applied by the internal tendons of the robotic tool is:

$$V_p = F_p\, sin\theta\, u(d,l) \quad (5)$$

in which F_p is the tendon-pulling force, and θ is the bending angle of the robotic tool. Replacing Equations (2) to (5) into Equation (1):

$$\begin{aligned}\Pi(u) = \int_0^l \frac{EI}{2}\left(\frac{\partial^2 u(d,z)}{\partial z^2}\right)^2 dz \\ + \frac{K}{2}\int_0^l (u(d,z) - u_t(d,z))^2\, dz \\ - F_t u(d,l) - F_p sin\theta\, u(d,l)\end{aligned} \quad (6)$$

To solve this equation, which results in the predicted deflected shape of the robotic tool, the Rayleigh-Ritz method is used [18]. The following finite series represent the weighted shape functions:

$$u_n(d,z) = \sum_{i=1}^{n} q_i(z) g_i(d) \quad (7)$$

in which $u_n(d,z)$ is the weighted shape function, $q_i(z)$ is the i^{th} shape function, and $g_i(d)$ is the corresponding weighting coefficient.

$q_i(z)$ the i^{th} vibration mode and can be found as:

$$q_i(z) = \frac{1}{k_i}\left(\sin\left(\beta_i \frac{z}{l}\right) - \sinh\left(\beta_i \frac{z}{l}\right) - \gamma_i\left[\cos\left(\beta_i \frac{z}{l}\right) - \cosh\left(\beta_i \frac{z}{l}\right)\right]\right) \tag{8}$$

in which γ_i and k_i are:

$$\gamma_i = \frac{sin\beta_i + sinh\beta_i}{cos\beta_i + cosh\beta_i} \tag{9}$$

$$k_i = sin\beta_i - sinh\beta_i - \gamma_i(cos\beta_i - cosh\beta_i) \tag{10}$$

where β_i is a constant. For a cantilever beam (clamped-free), $\beta_i = \pi(i - \frac{1}{2})$, and thereby β_1 to β_4 are 1.857, 4.695, 7.855, and 10.996, respectively.

By inserting the weighted shape function into Equation (6), the following equation is obtained:

$$\Pi(u_n) = \frac{EI}{2}\int_0^l \left(\sum_{i=1}^{n} q_i''(z) g_i(d)\right)^2 dz + \frac{K}{2}\int_0^l \left(\sum_{i=1}^{n} q_i(z) g_i(d) - u_t(d,z)\right)^2 dz - F_t \sum_{i=1}^{n} q_i(l)\, g_i(d) - F_p sin\theta \sum_{i=1}^{n} q_i(l)\, g_i(d) \tag{11}$$

in which $q_i''(z)$ denotes the second derivative of $q(z)$ with respect to z. The condition for minimizing the potential $\Pi(u_n)$ is $\frac{\partial \Pi}{\partial g_j} = 0$ for $j = 1, \ldots, n$.

$$\frac{\partial \Pi(u_n)}{\partial g_j(d)} = EI\int_0^l \left(\sum_{i=1}^{n} q_i''(z) g_i(d)\right) q_j''(z) dz + K\int_0^l \left(\sum_{i=1}^{n} q_i(z) g_i(d) - u_t(d,z)\right) q_j(z)\, dz - F_t - F_p sin\theta = 0 \tag{12}$$

Equation (12) can be simplified into:

$$\sum_{i=1}^{n} \varphi_{ji} g_i(d) - \omega_j - F_t - F_p sin\theta = 0 \tag{13}$$

in which

$$\varphi_{ji} = EI\int_0^l q_i''(z) q_j''(z) dz + K\int_0^l q_i(z)\, q_j(z) dz \tag{14}$$

$$\omega_j(z) = K\int_0^l u_t(d,z) q_j(z) dz \tag{15}$$

The simplified equation can be written in matrix form as:

$$\Phi(\mathrm{z}) g(\mathrm{d}) = F_t 1_{n\times 1} + F_p sin\theta 1_{n\times 1} + \Omega(z) \tag{16}$$

in which the matrices are:

$$\Phi = \begin{bmatrix} \varphi_{11} & \cdots & \varphi_{1n} \\ \vdots & \ddots & \vdots \\ \varphi_{n1} & \cdots & \varphi_{nn} \end{bmatrix}; \Omega = \begin{bmatrix} \omega_1 \\ \vdots \\ \omega_n \end{bmatrix}; g = \begin{bmatrix} g_1 \\ \vdots \\ g_n \end{bmatrix} \tag{17}$$

solving for g:

$$g = \Phi^{-1}(F_t 1_{n\times 1} + F_p sin\theta 1_{n\times 1} + \Omega) \tag{18}$$

Finally, the deflected shape of the tool can be obtained by inserting Equations (8) and (18) into Equation (7). This model is validated using active needle insertion experiments in soft tissue, explained in Section IVB.

III. Experiments

A. *Robotic System for Steering inside Soft Tissue with Real-Time Ultrasound Tracking*

The robotic needle insertion system, shown in Figure 3a, was used to insert and actuate the active needle inside a phantom tissue. The robotic system consists of (i) a needle manipulation system (Figure 3b), which comprises of a Maxon motor that is programmed to pull the tendons and actuate (bend) the active needle, (ii) US machine (Chison, ECO 5) and an Arducam USB camera (Figure 3c) to track the needle tip in real time, and (iii) a linear motorized stage (Velmex, Inc., Bloom- field, NY) and a guide template (Figure 3d) for axial movement (insertion) of the needle inside the tissue.

A robot-assisted ultrasound tracking (R-AUST) method was used in this work to track the needle tip in real time. Using 2D transverse US images, the R-AUST method visualizes the cross section of the needle using a series of imaging techniques to identify the coordinates of the needle tip. A Python code was programmed to analyze the images streaming from a USB port connected to a frame grabber (Epiphan Av.io HD, Epiphan Systems, Ottawa, Canada), and process them to capture the needle tip in real time. It is important for the US probe to move with the needle tip. Therefore, a motorized linear stage was assembled and programmed (actuated by another Maxon motor) to move the US probe on top of the needle tip during the needle insertion process. The Maxon motor was programmed in Python to change the US probe's velocity with respect to the needle insertion's velocity to ensure visibility of the needle tip in US images. For further detail please see our previous publications [10], [36].

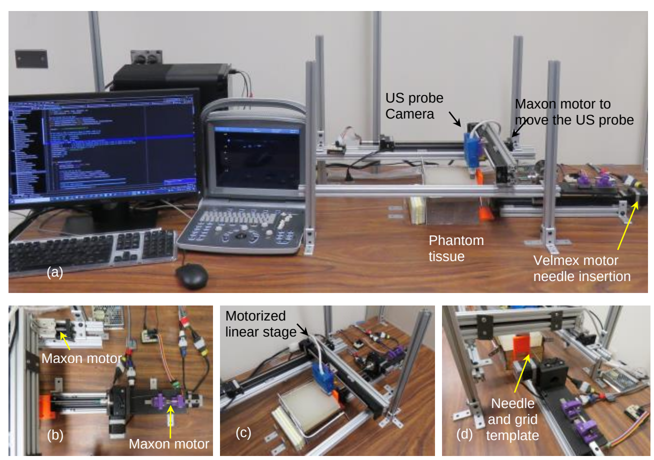

Figure 3. (a) Robotic needle insertion system consisting of (b) a needle manipulation (actuation) system to pull the tendons and bend the active needle, (c) a US probe and camera mounted on a linear stage for R-AUST of the needle tip in tissue, and (d) a linear stage and grid template for needle insertion.

B. *Multiple-Layer Phantom Tissue with Various Stiffness*

This section presents methods to extract properties of tissue using a nanoindentation device, as well as studies on needle insertion forces. Intraoperative information of tissue's localized Young's Modulus and needle insertion force is essential in developing a robotically steerable needle to reach the cancerous tissue with higher accuracy. In this work, three different phantom stiffnesses (regular, hard, and soft), and a bovine liver were analyzed to represent varying properties of the prostate tissue at different stages of cancer development. To give an estimation, a normal prostate gland is soft, elastic-like, with a relatively low Young's modulus (~30 kPa), while a cancerous prostate tissue is relatively stiff with a higher Young's modulus (~100 kPa). The phantom tissue stiffness data was used in comparison with the force a needle would exert when inserted into the phantom tissue.

The nanoindentation device (iNano, KLA Instruments), shown in Figure 4a, was used to measure and record mechanical properties of different types of phantom tissues. Figure 4b shows the sample mounted on the holder for indentation tests. Force and displacement data was recorded by creating small oscillations (making several punches) into the phantom tissues. The data was then used to estimate Young's modulus of each phantom tissue.

Figure 4. (a) Nanoindenter and (b) sample mounted on the holder for indentation test to find tissue properties.

A six-axis force and torque sensor (Nano 17, ATI Industrial Automation) was used to measure the needle insertion force exerted at the base of a bevel tip needle during a needle insertion task. The needle was placed perpendicular to the force sensor and moved at a constant speed of 1.0 mm/s. As the needle was inserted into the phantom tissue, there were deflections in the needle. The needle insertion force gradually increased while inserted deeper inside the tissue due to higher friction.

IV. Results and Discussion

A. Tissue Properties and Needle Insertion Force

Figures 5a to 5d show the needle insertion force vs. insertion depth for bovine liver, regular, soft, and hard phantom tissues, respectively. It was observed that the deeper the needle is inserted into the tissue, the greater force is applied due to increase in friction acting back on the needle. At the depth of 60mm, the hard phantom exerted a maximum force of 10.30N, and the bovine liver exerted a maximum force of 3.10N. The force measurements are used in the model to predict the needle deflection at different depths inside tissue. After recording force measurements of three different stiffnesses from one needle insertion, the 50-50% Hard-Regular tissue recorded a higher slope of 0.195 compared to the 50-50% Soft-Regular slope of 0.034 and the 100% Regular slope of 0.144.

The following Young's modulus were found for hard, regular, and soft phantom tissues, and the beef liver tissue using the nanoindenter device. Standard deviation was found by four repetitions.

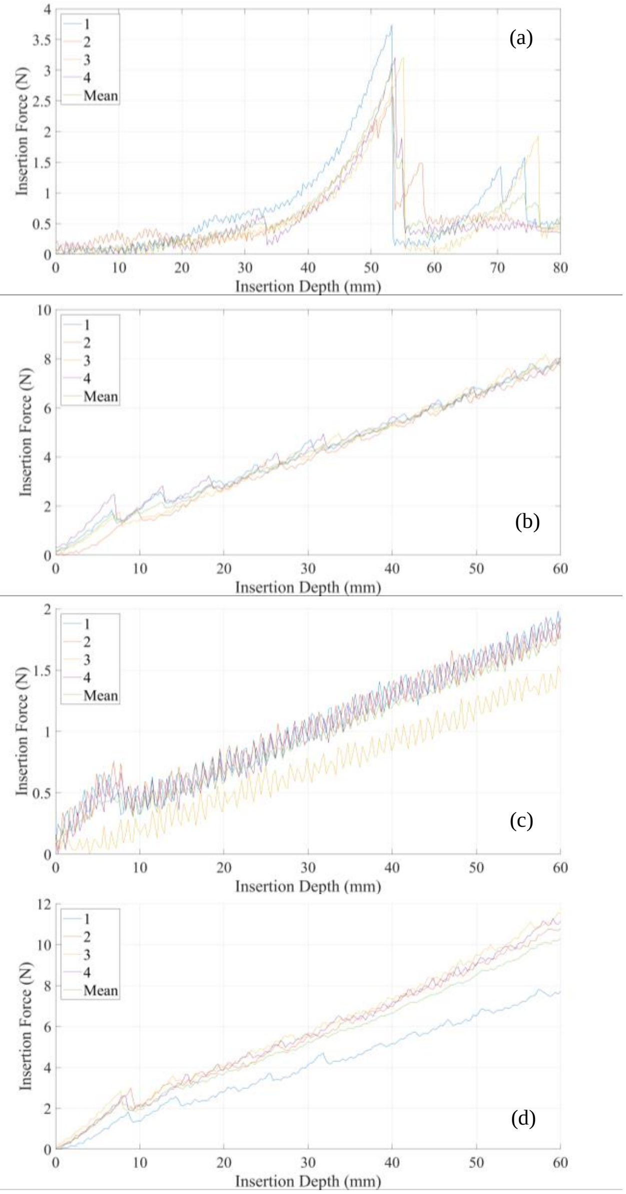

Figure 5. Force measurements in needle insertion experiments in (a) beef liver, and (b) regular, (c) soft, and (d) hard phantom tissues.

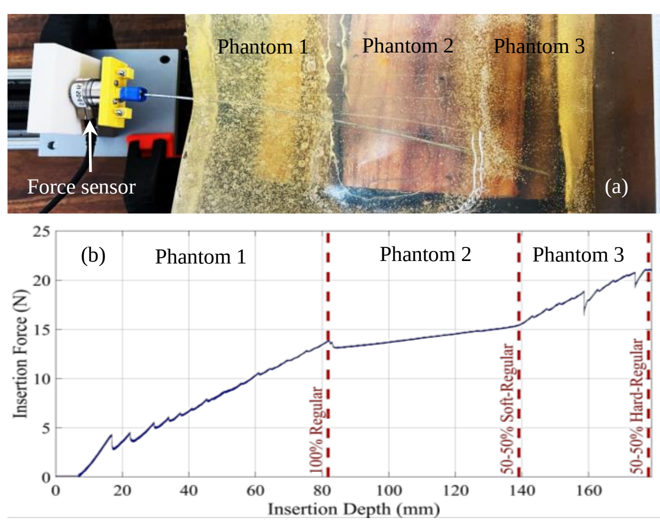

Figure 6. (a) Needle insertion inside a three-layer phantom tissue, and (b) needle insertion force.

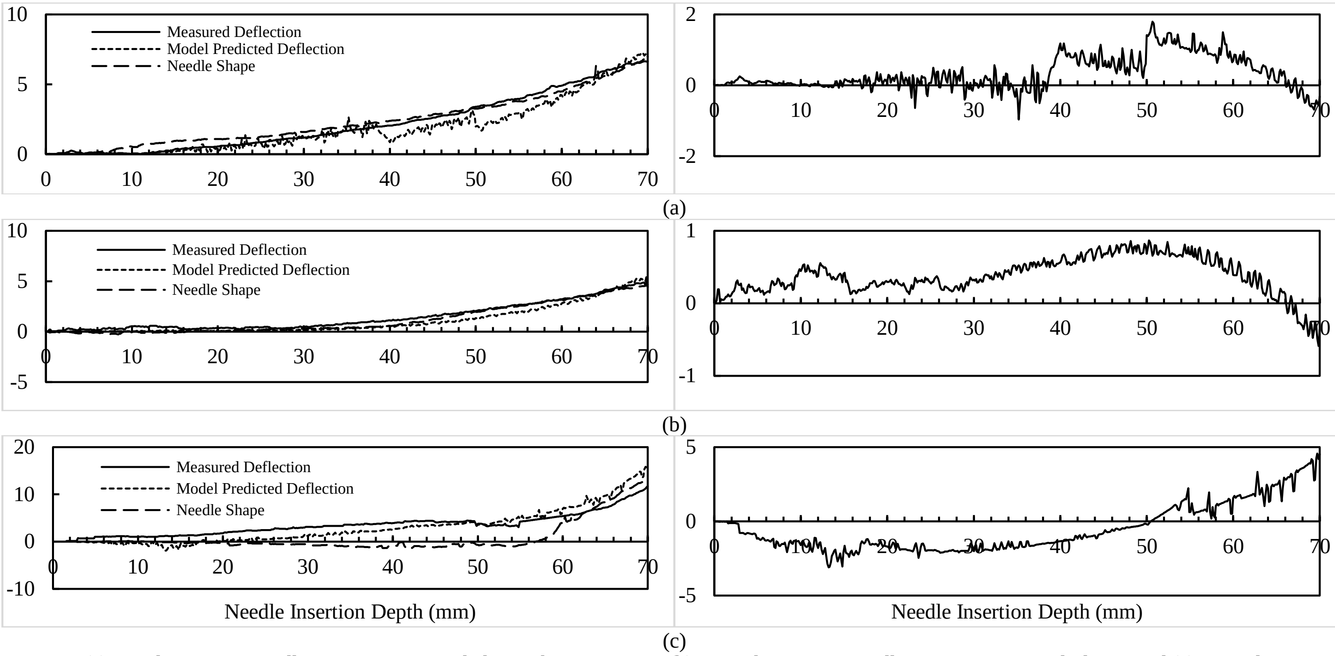

Figure 7. (a) Bevel-tip active needle insertion in a single layer phantom tissue, (b) conical-tip active needle insertion in a single-layer, and (c) conical-tip active needle insertion in a two-layer phantom tissues to a depth of 70mm. Needle total deflection is shown on the left, along with model prediction error on the right. Units are in mm.

Young's Modulus of the regular phantom tissue (with 100% regular elastomer) was estimated at 77.14±0.44kPa, which is comparable with a normal prostate tissue (~69±17kPa). Young's Modulus of the hard phantom tissue (with 50% hard and 50% regular elastomer) was estimated at 98.82±2.85kPa, which is comparable with a cancerous prostate tissue (~100±20kPa). Young's Modulus of the soft phantom tissue (with 50% soft and 50% regular elastomer) was estimated at 9.29±1.78kPa. Young's Modulus of the beef liver tissue was estimated at 14.39±4.51kPa. It was shown that a different combination of hardener and softener could be used to manipulate the phantom tissue's Young's modulus in the range of 9–98 kPa to mimic the properties of a prostate gland at different stages of cancer development.

Figure 6a shows the needle insertion setup to measure the needle insertion force in a three-layer phantom that was developed using 50% hard and 50% regular elastomers (Phantom 1), 50% soft and 50% regular elastomers (Phantom 2), and 100% regular elastomers (Phantom 3). The needle insertion force is plotted in Figure 6b, showing the force transitioning from one phantom to the other.

B. Model Validation: Active Needle Steering in Soft Tissue

This section evaluates the model prediction by directly comparing the estimated deflection of the needle (predicted by the model) with the measured deflection (provided by the R-AUST) and estimating the maximum and average error in shape prediction (difference between the predicted and measured needle deflection). The experiments have been performed for bevel-tip and conical-tip active needle insertion in a single-layer phantom tissue and a conical-tip active needle insertion in a two-layer phantom tissue.

Figure 7a (left) compares the estimated deflection of a bevel-tip active needle in a single-layer phantom tissue, predicted by the model, with the deflection of the needle measured (recorded) by the R-AUST. The maximum measured and estimated (model-predicted) deflections were 6.66mm, and 7.28mm, respectively at 70mm of insertion depth. Figure 7a (right) shows the error in needle deflection model prediction. The error was found by calculating the difference between the estimated (model-predicted) and measured needle deflections. The maximum error was 1.80mm, with an average error of 0.33mm.

A slightly larger error was observed at higher insertion depths. The tendon displacement and pulling force were applied gradually during the needle insertion to actuate the active needle. The tendon pulling force was estimated using the Maxon motor data collected from EPOS Studio during the needle insertion. The tendon pulling (needle actuation and the consequent bending) initiated at the depth of 13mm and ends at the 37mm of depth.

Table 2 lists the maximum deflection, maximum and average errors for three bevel-tip active needle insertion trials in a single-layer phantom tissue to a depth of 70mm. The maximum and average errors of model prediction for three needle insertion trials were 1.54±0.29mm, and 0.26±0.07mm, respectively. The maximum error was observed at instances with insufficient accuracy in the needle tip tracking.

Figure 7b (left) compares the estimated deflection of a conical-tip active needle in a single-layer phantom tissue, predicted by the model, with the deflection of the needle measured (recorded) by the R-AUST. The maximum measured and estimated (model-predicted) deflections were 5.00mm, and 5.58mm, respectively at 70mm of insertion depth. The conical tip (as expected) resulted in smaller deflection (displacement) at the needle tip. Figure 7b (right) shows the error in needle deflection model prediction. The absolute error was found by calculating the difference between the estimated (model-predicted) and measured needle deflections.

The maximum error was 0.87mm, with an average error of 0.38mm. A slightly larger error was observed at higher insertion depths (55mm to 70mm of depth). The tendon pulling (needle actuation and the consequent bending) initiated at the depth of 4mm and ends at the 15mm of depth.

Table 2 lists the maximum deflection, maximum and average errors for three conical-tip active needle insertion trials in a single-layer phantom tissue to a depth of 70mm. The maximum and average errors of model prediction for three needle insertion trials were 1.23±0.36mm, and 0.50±0.17mm, respectively.

Figure 7c (left) compares the estimated deflection of a conical-tip active needle in a two-layer phantom tissue (Trial 1), predicted by the model, with the deflection of the needle measured (recorded) by the R-AUST. The maximum measured and estimated (model-predicted) deflections were 11.74mm, and 16.26mm, respectively at 70mm of insertion depth.

Figure 7c (right) shows the error in needle deflection model prediction. The error was found by estimating the difference between the estimated (model-predicted) and measured needle deflections. The maximum error was 4.57mm, with an average error of 0.52mm. The tendon pulling (needle actuation and the consequent bending) initiated at the depth of 4mm and ends at the 15mm of depth.

Table 2. Summary of active needle insertion experiments (three trials) in phantom tissues to a depth of 60mm.

Bevel-tip active needle insertion in a single-layer tissue

Trial	Max deflection model prediction / measured (mm)	Max error (mm)	Average error (mm)
1 (Figure 7a)	7.28 / 6.66	1.80	0.33
2	7.35 / 5.80	1.60	0.20
3	7.86 / 6.80	1.22	0.24
Conical-tip active needle insertion in a single-layer tissue			
1 (Figure 7b)	5.58 / 5.00	0.87	0.38
2	9.01 / 5.30	1.63	0.16
3	6.32 / 5.63	1.20	0.50
Conical-tip active needle insertion in a two-layer tissue with R-AUST			
1 (Figure 7c)	16.26 / 11.74	4.57	0.52
2	15.67 / 11.75	4.14	0.07
3	12.83 / 9.75	3.39	0.17

Table 2 lists the maximum deflection, maximum and average errors for three conical-tip active needle insertion trials in a two-layer phantom tissue to a depth of 70mm. The maximum and average errors of model prediction for three needle insertion trials were 4.03±0.59mm, and 0.25±0.23mm, respectively using the sole R-AUST method.

Inaccurate US tracking was observed close to the margin where the two phantom tissues of different properties bonded. It was noticed that during the needle insertion whenever the needle passed by the different tissue stiffness division, it compressed the phantom tissues, which created a space between the US probe and the tissue, and injected inaccuracies in US tracking. This was observed in all three trials of needle insertions in two-layer phantom tissue.

Inaccurate tracking can introduce major error in model prediction. In a previous work [36], we introduced an improved tracking method, which integrates the R-AUST with shape prediction of the needle's curvature (curve fitting to three US images) to accurately track the needle deflection in real time. We showed previously [36] that this method results in tracking with excellent accuracy (average error of 0.37mm). Application of this method results in a more accurate overall tracking, and consequently a more accurate overall prediction of the model for needle deflection. The trend shows that application of R-AUST along with shape prediction (improved tracking) to a wider insertion interval result in a more accurate tracking and a more accurate model prediction.

In summary, the model was able to predicts the needle deflection with an average error of 0.26±0.07mm and 0.50±0.17mm for bevel-tip and conical-tip active needle insertion in single-layer phantom tissue, respectively, and an average error of 0.25±0.23mm for the conical-tip active needle insertion in two-layer phantom tissue. Real-time tracking of the needle tip was challenging especially in needle insertions in two-layer tissue. Inaccurate tracking could be compensated for using a previously developed R-AUST method integrated with needle shape prediction.

V. CONCLUSION

This work introduced a new model for bending deflection of an active steerable continuum robot inside soft tissue. The model was validated via insertion and manipulation experiments. In future work, we will use this model in closed loop model-based control for tool navigation inside tissue. Future work also includes further development of this model with more complex tissue (e.g., various stiffness, viscoelastic properties, etc.) to have a model closer to real tissue. We also plan to perform insertion and manipulation experiments in different ex-vivo and in-vivo tissues. We conclude that the model can predict tendon-driven active needle deflection inside a multiple-layer soft tissue with reasonable accuracy.

ACKNOWLEDGMENT

Research reported in this publication was supported by the National Institute of Biomedical Imaging and Bioengineering of the National Institutes of Health under Award Number K25EB030562. The content is solely the responsibility of the authors and does not necessarily represent the official views of the National Institutes of Health.

The authors would like to thank Chris Pham for his contributions on extraction of tissue properties during his summer internship in our lab.

REFERENCES

[1] T. A. Brumfiel, A. Sarma, and J. P. Desai, “Towards FBG-based End-Effector Force Estimation for a Steerable Continuum Robot,” *Int. Symp. Med. Robot.*, 2022.

[2] T. E. Ertop *et al.*, “Towards Suturing from Within the Urethra Using Concentric Tube Robots: First Experiences in Biological Tissues,” *2022 Int. Symp. Med. Robot. ISMR 2022*, 2022, doi: 10.1109/ISMR48347.2022.9807548.

[3] T. L. De Jong, N. J. van de Berg, L. Tas, A. Moelker, J. Dankelman, and J. J. van den Dobbelsteen, “Needle placement errors: Do we need steerable needles in interventional radiology?,” *Med. Devices Evid. Res.*, vol. 37, no. 3, pp. 259–265, 2017, doi: 10.2147/MDER.S160444.

[4] J. Burgner-Kahrs, D. C. Rucker, and H. Choset, “Continuum Robots for Medical Applications: A Survey,” *IEEE Trans. Robot.*, vol. 31, no. 6, pp. 1261–1280, 2015, doi: 10.1109/TRO.2015.2489500.

[5] S. Karimi and B. Konh, “Self-Sensing Feedback Control of Multiple Interacting Shape Memory Alloy Actuators in a 3D Steerable Active Flexible Needle,” *J. Intell. Mater. Syst. Struct.*, vol. 31, no. 12, pp. 1524–1540, 2020.

[6] S. Karimi and B. Konh, “Kinematics Modelling and Dynamics Analysis of an SMA-Actuated Active Flexible Needle for Feedback-Controlled Manipulation in Phantom,” *Med. Eng. Phys.*, 2022.

[7] B. Konh, B. Padasdao, Z. Batsaikhan, and J. Lederer, “Steering a Tendon-Driven Needle in High-Dose-Rate Prostate Brachytherapy for Patients with Pubic Arch Interference,” in *International Symposium on Medical Robotics (ISMR)*, 2021, pp. 1–7.

[8] B. Padasdao, Z. K. Varnamkhasti, and B. Konh, “3D Steerable Biopsy Needle with a Motorized Manipulation System and Ultrasound Tracking to Navigate inside Tissue,” *J. Med. Robot. Res.*, vol. 05, no. 03n04, pp. 2150003-1-2150003–18, 2021, doi: 10.1142/S2424905X21500033.

[9] B. Padasdao, Z. Batsaikhan, S. Lafreniere, M. Rabiei, and B. Konh, “Modeling and Operator Control of a Robotic Tool for Bidirectional Manipulation in Targeted Prostate Biopsy,” in *International Symposium on Medical Robotics (ISMR)*, 2022, pp. 1–7.

[10] B. Konh, Z. Batsaikhan, and B. Padasdao, “3D shape estimation of an active needle inside tissue using 2D ultrasound images,” in *Design of Medical Devices Conference*, 2021, pp. 1–4.

[11] B. Konh, B. Padasdao, Z. Batsaikhan, and S. Y. Ko, “Integrating robot-assisted ultrasound tracking and 3D needle shape prediction for real-time tracking of the needle tip in needle steering procedures,” *Int. J. Med. Robot. Comput. Assist. Surg.*, vol. 17, no. 4, 2021, doi: 10.1002/rcs.2272.

[12] B. Padasdao, Z. Batsaikhan, D. Brown, and J. Moore, “Estimation of tissue movement in needle insertion tasks using an active needle,” in *Design of Medical Devices Conference*, 2022, pp. 1–5.

[13] S. Misra, K. B. Reed, B. W. Schafer, K. T. Ramesh, and A. M. Okamura, “Mechanics of flexible needles robotically steered through soft tissue.,” *Int. J. Rob. Res.*, vol. 29, no. 13, pp. 1640–1660, 2010, doi: 10.1177/0278364910369714.

[14] N. V. Datla *et al.*, “A model to predict deflection of bevel-tipped active needle advancing in soft tissue,” *Med. Eng. Phys.*, vol. 36, no. 3, pp. 285–293, 2014, doi: 10.1016/j.medengphy.2013.11.006.

[15] T. Lehmann, R. Sloboda, N. Usmani, and M. Tavakoli, “Model-Based Needle Steering in Soft Tissue via Lateral Needle Actuation,” *IEEE Robot. Autom. Lett.*, vol. 3, no. 4, pp. 3930–3936, 2018, doi: 10.1109/LRA.2018.2858001.

[16] B. Padasdao, S. Lafreniere, M. Rabiei, Z. Batsaikhan, and B. Konh, “Teleoperated and Automated Control of a Robotic Tool for Targeted Prostate Biopsy,” *Jounral Med. Robot. Res.*, pp. 1-24 under review, 2022.

[17] R. C. Hibbeler, *Mechanics of Materials*. Prentice Hall, 2008.

[18] T. Lehmann, C. Rossa, N. Usmani, R. Sloboda, and M. Tavakoli, “Deflection modeling for a needle actuated by lateral force and axial rotation during insertion in soft phantom tissue,” *Mechatronics*, vol. 48, pp. 42–53, 2017, doi: 10.1016/j.mechatronics.2017.10.008.

[19] Z. K. Varnamkhasti, B. Konh, O. H. Maghsoudi, Y. Yu, and L. Liao, “Ultrasound Needle Tracking Inside a Soft Phantom and Methods to Improve the Needle Tip Visualization,” in *Design of Medical Devices Conference*, 2019, pp. 1–6.

[20] R. J. Roesthuis, M. Abayazid, and S. Misra, “Mechanics-based model for predicting in-plane needle deflection with multiple bends,” *2012 4th IEEE RAS EMBS Int. Conf. Biomed. Robot. Biomechatronics*, pp. 69–74, 2012, doi: 10.1109/BioRob.2012.6290829.

[21] R. G. Budynas, J. K. Nisbett, and J. E. Shigley, *Shigley’s mechanical engineering design*. 2018.